Oxygen Electrocatalysis by α-MnO_2/Mn_3O_4/CeO_2/C: Unravelling the Role of CeO_2 in the Stabilization of Multivalent Mn Species on α-MnO_2/Mn_3O_4/CeO_2/C Surface for Enhanced Electrocatalysis*

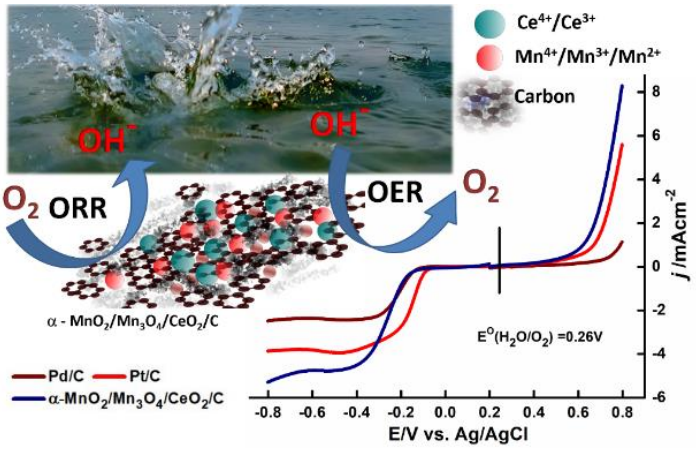

This chapter comprises the study of the effect of CeO_2 in boosting the bifunctional ORR and OER activity of α-MnO_2/Mn_3O_4/C. To investigate the electrocatalytic properties comprehensively and systematically α-MnO_2/Mn_3O_4/C, α-MnO_2/Mn_3O_4/CeO_2/C and CeO_2/C ECs were synthesized via a facile two-step solvothermal approach followed by calcination at 450 °C for 4 h. The α-MnO_2/Mn_3O_4/CeO_2/C demonstrated excellent bifunctional ORR and OER activity with appreciable durability and stability. The effect of CeO_2 concentration (relative to α-MnO_2/Mn_3O_4) was further explored with the electrocatalytic activity of α-MnO_2/Mn_3O_4/CeO_2/C-37 and α-MnO_2/Mn_3O_4/CeO_2/C-73 ECs that was synthesized by same method. The physicochemical and electrochemical properties of the as-prepared ECs were evaluated using various analytical techniques which are discussed in this chapter. The details of the material synthesis and experimental methodologies are included in the experimental section: Chapter 2.

*The content of this chapter has been published in "*Energy & Fuels*, 35(13):10756-10769, 2021"

6.1. Introduction

Efficient ORR, as well as the OER process, is crucially significant for new generation energy storage and conversion devices including fuel cells, metal-air batteries etc. [1-3]. Since the reduction of O_2 is an uphill process with a high-energy barrier, appropriate ECs are entailed for this process to occur at a sensible rate. The sluggish ORR in fuel cells and metal-air batteries is an imminent concern and hinders the commercial execution of this anticipative technology. Furthermore, cultivating the efficiency of the ORR and the OER lingers as the major challenge. Electrochemical conversion between O_2, H_2, H_2O_2 and H_2O using nano-electrocatalysts has become apparent as the most viable and attractive way to escalate the slow kinetics of electrode reaction. Electrocatalytic reduction of O_2 has stood out as a potential mechanism for enhancing fuel cell performances in recent years [4-7]. ORR and OER proceed through a process with the transfer of electrons establishing typical reaction intermediates and mechanisms. Consequently, perplexity appears in designing an effective bifunctional EC for both processes [8–10]. Pt and its composite materials are recognized to be the best ORR ECs, but they are expensive and have poor stability caused by intricate degradation processes during long-run electrochemical operations [11–16]. Ir and Ru oxides, on the other hand, exhibits astonishing OER activities but are expensive and poor ORR ECs [17]. These drawbacks critically restrict the unitization of energy conversion systems thereby hindering product commercialization. Consequently, non-noble metal-based ECs for the ORR/OER with high efficiency and stability are exceedingly desirable.

A bifunctional oxygen EC that can efficiently catalyze the ORR/OER processes is of great importance for fuel cells and metal-air batteries. Over the past decade, various MOs such as MnO_x, Fe_2O_3, Co_3O_4, etc. have been extensively investigated for ORR and OER processes due to the merit of their low cost and easy availability [18–20]. Among them, MnO_x with its mixed valence states (Mn^{2+}, Mn^{3+}, Mn^{4+}) has received enormous attention in electrocatalysis. Diverse chemical compositions, crystalline structure and rich oxidation states of MnO_x are classes of inherent properties that make them a group of promising ORR ECs in alkaline medium [21,22]. Recently, the electrocatalytic performance of α-MnO_2 nanowire has been reported in terms of overall ORR activity which is dependent on surface Mn^{3+}

concentration and the covalent nature of the Mn-O bonds [23]. The intensified surface Mn^{3+} concentration and the increased covalent nature of the Mn-O bond significantly enhance the ORR activity. Ryabova *et al.* described an inclusive electrocatalytic study on a set of MnO_x comprising MnO_2, Mn_2O_3, Mn_3O_4, MnOOH and B-site Mn perovskites and evaluate the impact of surface Mn^{4+}/Mn^{3+} redox transition for specific ORR activity [24]. Nevertheless, MnO_x faces few challenges in the ORR process due to its deficient intrinsic electrical conductivity and ability to inadequate oxygen adsorption [21,25].

Carbon-based materials, e.g., carbon nanotube, Vulcan XC 72R, ketjenblack, BP2000, graphene, etc. exhibit unique conductive as well as surface properties that can enrich the performance of electrocatalytically active materials. They have been extensively investigated as cathode components for metal-air batteries [26–29]. TMOs, MTMOs and mixed valence transition-inner transition MOs (MTITMOs) are some important classes of ECs that exhibit better ORR/OER performance in alkaline electrolytes. Recently, carbon-supported TMOs, MTMOs and MTITMOs-centered materials are found to be promising alternatives to expensive Pt-based ECs [30–36].

CeO_2 has unique characteristics such as high oxygen storage capability, high reactivity and hardness, high oxygen ionic conductivity, strong ultraviolet radiation absorption ability as well as high stability at high temperatures. Over the past few decades, CeO_2 has been utilized in different catalytic processes and has attracted enormous attention as an 'active EC' as well as an 'active supporter/promoter' [37]. Owing to its fascinating Ce^{4+}/Ce^{3+} redox couple, CeO_2 has also been extensively used as an active catalyst/promoter in several reactions such as CO oxidation, ORR, elimination of toxic exhaust (SO_2, CO, and NO_x, three-way catalysis), selective hydrogenation of unsaturated aldehydes and isobutane dehydrogenation and as free radical scavenger [37–41]. Recently CeO_2 promoted TMOs on carbon have been used as bifunctional ECs for ORR and OER [22,42–44] Scrutinizing the need for high activity with greater stability for energy storage and conversion technologies, here we report the electrocatalytic ORR and OER activity of α-MnO_2/Mn_3O_4 doped hybrid CeO_2/C nanostructure as a non-precious EC.

6.2. Results and Discussion

6.2.1. Characterization of the synthesised ECs

The structural changes, crystallinity and phase purity were investigated by using powder XRD analysis. Figure 6.1. a show the XRD patterns of Vulcan carbon, α-MnO_2/Mn_3O_4/C, α-MnO_2/Mn_3O_4/CeO_2/C and CeO_2/C. The broad peak with low intensity at about 24° (2θ) shown by Vulcan carbon is the characteristic peak of graphitic sp^2 carbon structure [45]. The peak vanishes in MnO_x/C, MnO_x/CeO_2/C and CeO_2/C lattices indicating high dispersion of carbon phases into the MO latices. The CeO_2/C sample displayed a clear diffraction pattern of pure CeO_2 (JCPDS No. 81-0792), while the MnO_x/C sample exhibited mixed diffraction peaks of α-MnO_2 (JCPDS No. 44-0141) and Mn_3O_4 (JCPDS No. 89-4837).

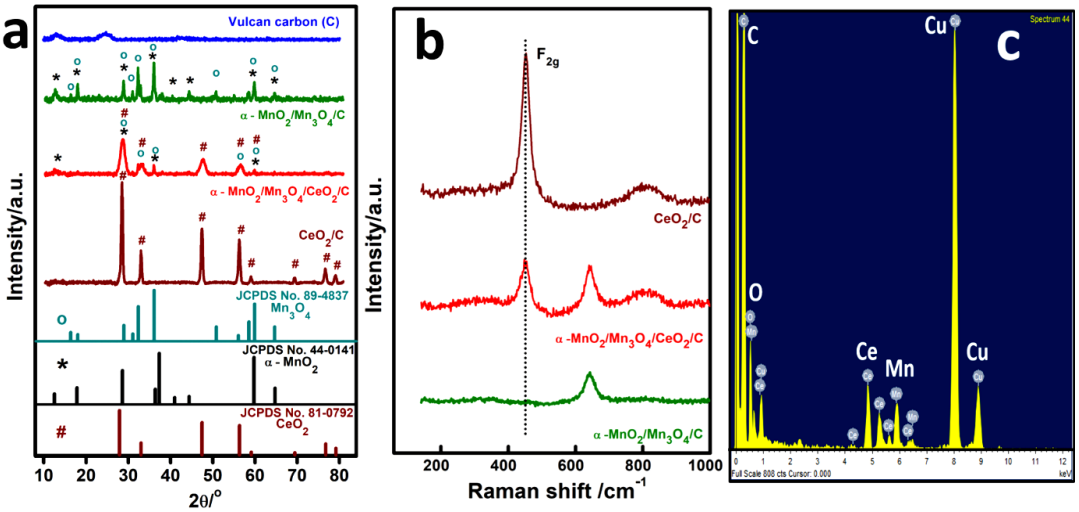

Figure 6.1. a) XRD patterns of Vulcan carbon, α-MnO_2/Mn_3O_4/C, α-MnO_2/Mn_3O_4/CeO_2/C and CeO_2/C (The symbols o, * and # represent the peaks corresponding to Mn_3O_4, α-MnO_2, and CeO_2, respectively), b) Raman spectra of CeO_2/C, α-MnO_2/Mn_3O_4/C and α-MnO_2/Mn_3O_4/CeO_2/C ECs, and c) EDX pattern of α-MnO_2/Mn_3O_4/CeO_2/C.

Similarly, the diffraction patterns of the MnO_x/CeO_2/C sample showed peaks for all CeO_2 (JCPDS No. 81-0792), α-MnO_2 (JCPDS No. 44-0141) and Mn_3O_4 (JCPDS No. 89-4837) suggesting the coexistence of the mixed hybrid. This observation establishes that there exists a partial and random interfacial overlapping phase in between all the CeO_2, α-MnO_2 and Mn_3O_4 phases instead of dispersion of α-MnO_2 and Mn_3O_4 phases into the CeO_2 lattice thereby developing

α-MnO_2/Mn_3O_4/CeO_2/C hybrid structure. Moreover, the change in peak intensity of the parent α-MnO_2/Mn_3O_4/C crystal lattice is likely affected by the addition of CeO_2 which endorses the incorporation of overlapping interfaces.

To study the structural changes and the effect of CeO_2 concentration in the α-MnO_2/Mn_3O_4/CeO_2/C hybrid, Raman spectroscopy analyses has been performed. Figure 6.1. b shows the Raman spectra of α-MnO_2/Mn_3O_4/CeO_2/C hybrid along with α-MnO_2/Mn_3O_4/C and CeO_2/C. The Raman spectrum of CeO_2/C show a sharp peak at about 454 cm^{-1} which is ascribed to the symmetric F_{2g} mode for *fcc* CeO_2 due to the symmetric O–Ce–O stretching over the surrounding oxygen atoms of the fluorite structured CeO_2 [40,46]. The observed significant broadening of the Raman F_{2g} peak with increasing Mn concentration suggests the establishment of more oxygen vacancy as the F_{2g} mode is highly labile to the disorder in the vicinity of oxygen sublattice [47]. The α-MnO_2/Mn_3O_4/CeO_2/C exhibit a band at 646 cm^{-1}, which can be ascribed to the characteristics Mn–O–Mn peak. It is well established and reported in the literature that the density of oxygen vacancies in ECs is a significant factor in the enhancement of the electrocatalytic ORR and OER processes.

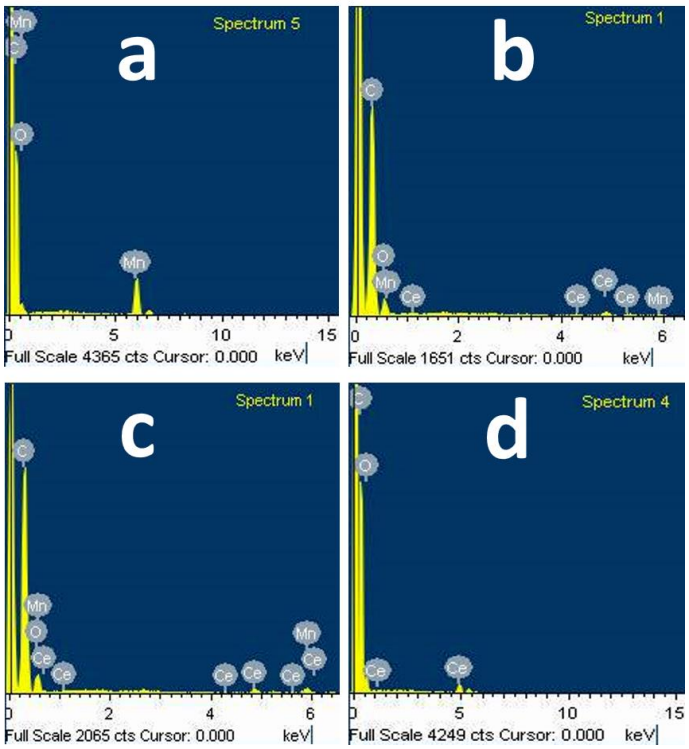

Figure 6.2.: EDX spectra of the ECs. a) α-MnO_2/Mn_3O_4/C, b) α-MnO_2/Mn_3O_4/CeO_2/C-37, c) α-MnO_2/Mn_3O_4/CeO_2/C-73 and d) CeO_2/C.

The elemental analysis and atomic percentages in α-MnO_2/Mn_3O_4/CeO_2/C were performed by EDX (Figure 6.1. c). The atomic percentages of Mn, Ce, O and C in α-MnO_2/Mn_3O_4/CeO_2/C were 1.40, 1.96, 3.11 and 73.88 % respectively. Cu peaks observed in the EDX spectrum appear due to the sample holder (carbon-coated copper grid) used during the measurement. EDX spectra and percentage compositions of the associated investigated ECs are summarized in Figure 6.2 and Table 6.1., respectively.

Table 6.1. Wt.% and At.% of the elements present in the ECs.

Elements	α-MnO_2/ Mn_3O_4/C		α-MnO_2/Mn_3O_4/ CeO_2/C-37		α-MnO_2/Mn_3O_4/ CeO_2/C		α-MnO_2/Mn_3O_4/ CeO_2/C-73		CeO_2/C	
	Wt.%	At.%	Wt.%	At.%	Wt.%	At.%	Wt.%	At.%	Wt.%	At.%
Mn	11.6	2.81	0.64	0.15	5.97	1.74	2.19	0.53	–	–
Ce	–	–	4.65	0.44	21.3	2.4	2.84	0.27	10.69	1.04
O	18.36	15.90	20.38	16.77	3.86	3.8	21.82	18.15	8.37	7.13
C	70.48	81.29	74.33	82.43	68.87	91.9	73.15	81.05	80.95	91.83

The spatial distribution of chemical composition and elements were further explored through the HAADF-STEM image. Figure 6.3 a, show the mapping distribution elements of the hybrid structure. The layered HAADF-STEM image of Mn, Ce and C in the same region is displayed in Figure 6.3 b suggesting homogeneous overlapping of Mn and Ce particles over the carbon matrix. Figure 6.3 c, d and e show the HAADF-STEM image of Mn, Ce and C, respectively indicating that elements Mn, Ce and C are uniformly distributed in the nanohybrid.

To study the morphology of α-MnO_2/Mn_3O_4 and CeO_2 NPs aggregation in the hybrid EC, TEM analysis has been performed. Figure 6.4 (a-c) display a low-resolution TEM image of the α-MnO_2/Mn_3O_4/CeO_2/C hybrid revealing the homogeneous distribution of α-MnO_2, Mn_3O_4 and CeO_2 NPs over carbon which also demarcates interfaces randomly distributed at the microscopic level. The overlying interfaces between α-MnO_2, Mn_3O_4 and CeO_2 nanostructures over the carbon matrix can be seen from the HR-TEM images as presented in Figure 6.4. d and e. Typical interplanar spacing of about 0.25 nm, 0.24 nm and 0.33 nm is obtained from the HRTEM image which is assigned to the (211) crystal planes of Mn_3O_4, (211) planes the HRTEM image is assigned to the (211) crystal planes of Mn_3O_4, (211) planes of α-MnO_2 nanostructures and (002) planes of carbon respectively [48-50] Another

observed typical interplanar spacing of about 0.31 nm can be assigned to the (111) crystal planes of CeO_2 [41]. The selected area electron diffraction (SAED) pattern assessed for α-MnO_2/Mn_3O_4/CeO_2/C displayed multiple diffraction rings that can be assigned to the crystalline reflections of (111)-CeO_2, (211)-Mn_3O_4, (211)-α-MnO_2, (521)-α-MnO_2 and (311)-CeO_2, as shown in Figure 6.4. c. SAED pattern further reveals a relatively better crystallinity and the presence of different phases in several

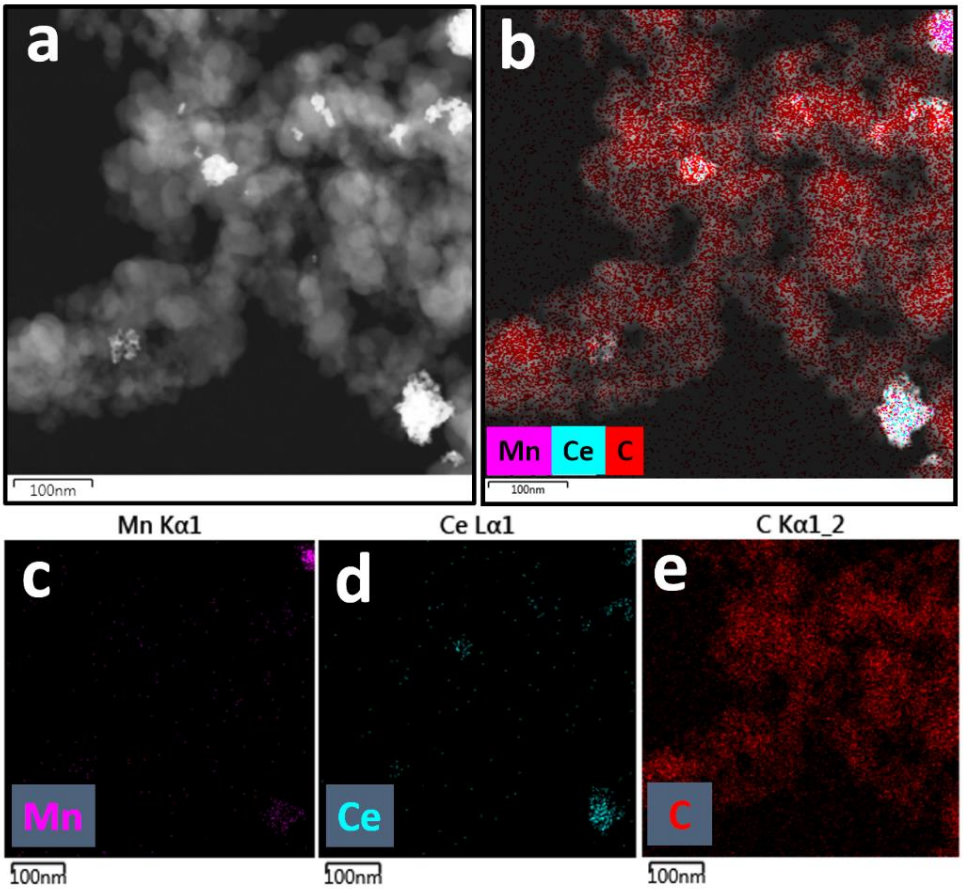

Figure 6.3. High-angle annular dark-field scanning transmission electron microscopy (HAADF-STEM) image and the mapping distribution of α-MnO_2/Mn_3O_4/CeO_2/C hybrid nanostructure (a), layered image (b), Mn (c), Ce (d) and carbon (e).

orientations for EC α-MnO_2/Mn_3O_4/CeO_2/C. The distinct lattice fringe in HR-TEM images and the SAED ring patterns shown in Figure 6.3.4 (c-e) suggest a better crystallinity of the synthesized nanostructured materials which is well consistent with the XRD patterns. The average diameter of nanoparticles was determined from the particle size distribution analysis of the α-MnO_2/Mn_3O_4/CeO_2/C image, suggesting

that the sizes are in the range of 3-12 nm where the average particle size is found to be 6 nm (Figure 6.4. f).

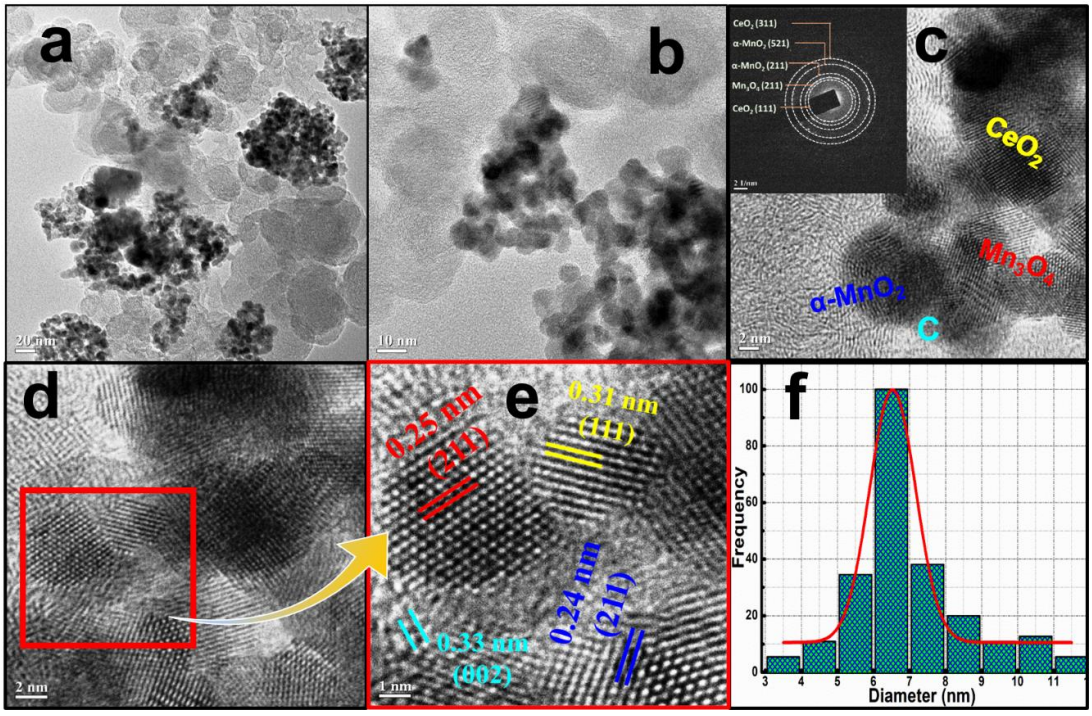

Figure 6.4. a-e) TEM and HRTEM images and SAED pattern (inset of c) of α-MnO_2/Mn_3O_4/CeO_2/C hybrid nanostructure, and f) particle size distribution of α-MnO_2/Mn_3O_4/CeO_2/C evaluated from the TEM image (b).

The surface compositions and the valence states of the α-MnO_2/Mn_3O_4/C, α-MnO_2/Mn_3O_4/CeO_2/C and CeO_2/C nanostructures were further investigated by XPS. The survey spectrum and core-level XPS spectrum of Mn 2p, O 1s, Ce 3d and C 1s of the ECs are presented in Figure 6.5. As shown in Figure 6.5b, Mn 2p XPS spectra were deconvoluted into three peaks in the binding energy (BE) of 636–650 eV, indicating the presence of variable oxidation states of Mn in the EC. It can be seen that the Mn $2p_{3/2}$ peak is rather broad, which could be attributed to the cohabitation of different Mn $2p_{3/2}$ levels viz. Mn^{2+}, Mn^{3+}, and Mn^{4+} species at the interfacial EC [51]. The BE at about 645.8, 642.4 and 639.4 eV can be assigned to Mn^{4+}, Mn^{3+} and Mn^{2+} respectively [52,53]. In the α-MnO_2/Mn_3O_4/CeO_2/C hybrid EC, a significant shift appears towards higher BE in all Mn oxidation states which suggests that there exists a strong interaction between MnO_x and CeO_2 species in the interfacial domain [54]. The percentage composition of Mn^{x+} in the α-MnO_2/Mn_3O_4/CeO_2/C heterostructure

was calculated from the deconvolution peaks and obtained as 27.9, 49.2 and 22.9%, respectively for Mn^{2+}, Mn^{3+} and Mn^{4+}. The O 1s XPS spectrum is presented in Figure 6.5 c shows typical features that rely on both the chemisorbed oxygen species (O_{ads}) and the lattice oxygen (O_{lat}). As a whole, the peak at 532.6 eV corresponds to O_{ads}, whereas the peak at 531.7 eV can be assigned to O_{lat} [55]. Due to the structural morphology and difference in electronegativity, a slight shifting of O_{lat} peaks is observed in the case of α-MnO_2/Mn_3O_4/CeO_2/C and CeO_2/C.

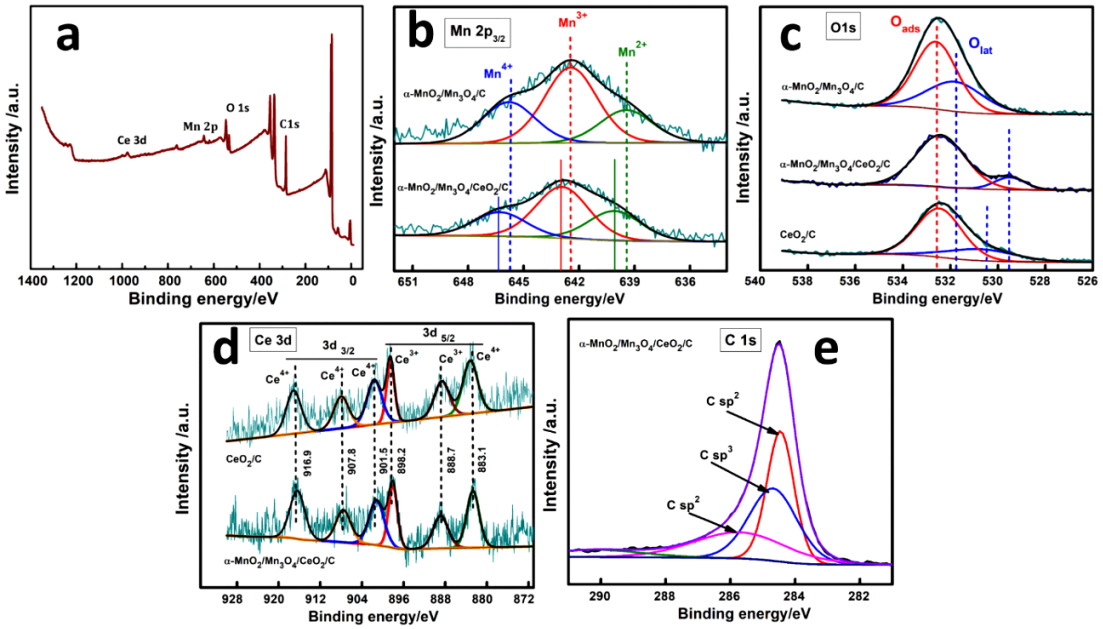

Figure 6.5. a) XP survey spectrum and core-level XP spectrum of Mn 2p of α-MnO_2/Mn_3O_4/C and α-MnO_2/Mn_3O_4/CeO_2/C (b), O 1s of α-MnO_2/Mn_3O_4/C, α-MnO_2/Mn_3O_4/CeO_2/C and CeO_2/C (c), Ce 3d of α-MnO_2/Mn_3O_4/CeO_2/C and CeO_2/C (d) and C 1s of α-MnO_2/Mn_3O_4/CeO_2/C (e).

The surface oxidation states of Ce in α-MnO_2/Mn_3O_4//C, α-MnO_2/Mn_3O_4/CeO_2/C and CeO_2/C were also investigated through XPS measurement. The deconvoluted peaks of the Ce 3d region produce two sets of peaks, which are assigned to $3d_{3/2}$ and $3d_{5/2}$ as shown in Figure 6.5 d. Usually, Ce in CeO_2 populates as Ce^{3+} and Ce^{4+} oxidation states. The peaks at 888.8 and 898.2 eV in the XP spectrum are assigned to Ce^{3+} while the peaks at 883.1, 901.5, 907.8, and 916.9 eV are assigned to the Ce^{4+} state of cerium [56,57]. It is noteworthy that the 3d (Ce^{3+} and Ce^{4+}) BE of α-

$MnO_2/Mn_3O_4/CeO_2/C$ are slightly lower than those of pure CeO_2/C as appears in the XPS spectrum. The minor shifts in the Ce 3d BE can be attributed to an increase in electron density in the vicinity of the Ce cation. The Ce^{3+} concentration is the key factor that determines the oxygen vacancies assorted in the ECs. The feasibility and enhancement of the $Ce^{4+} \leftrightarrow Ce^{3+}$ redox transition entirely rely on the oxygen vacancy density. The concentration of Ce^{3+} and Ce^{4+} was calculated for α-$MnO_2/Mn_3O_4/CeO_2/C$ heterostructure and was found to be 23.24 and 76.76% respectively. The result portrays that the α-$MnO_2/Mn_3O_4/CeO_2/C$ heterostructure is incorporated with adequately rich oxygen vacancies that might carry a significant role in the ORR/OER process. The C 1s spectrum deconvolution peak shows the C state in the α-$MnO_2/Mn_3O_4/CeO_2/C$ ECs (Figure 6.5 e). The sp^2 hybridization states in C 1s spectra specify the graphitic carbon concentration in the EC which is consistent with the XRD results. The calculated percentages of state composition of all the investigated ECs are presented in Table 6.2.

Table 6.2. Percentage composition of all states present in the catalysts.

Catalyst	Ce^{3+} (%)	Ce^{4+} (%)	Mn^{2+} (%)	Mn^{3+} (%)	Mn^{4+} (%)	O_{lat} (%)	O_{ads} (%)	C sp^2 (%)	C sp^3 (%)
α-$MnO_2/Mn_3O_4/C$	–	–	27.5	50.55	21.9	36.5	63.5	81.8	18.3
α-$MnO_2/Mn_3O_4/CeO_2/C$	23.4	76.76	27.9	49.2	22.9	12.9	87.1	63.2	36.7
CeO_2/C	39.4	60.6	–	–	–	26.3	73.7	91.6	8.4

To characterize the specific surface area and pore-size distribution of the series of investigated ECs, N_2 adsorption-desorption analyses were performed. A typical type-IV isotherm and H3-type hysteresis loop were observed for all the ECs (Figure 6.6 a-c). The insets of Figure 6.6. a-c display the respective pore size distribution curves, obtained by the BJH method, which suggests the characteristics mesoporous nature of the ECs. The calculated pore diameter was 2.8 nm for α-$MnO_2/Mn_3O_4/C$, 2.7 nm for CeO_2/C and 1.5 nm for α-$MnO_2/Mn_3O_4/CeO_2/C$ hybrid heterostructure. The specific surface area was calculated using the multipoint BET method and it is observed the specific surface area of α-$MnO_2/Mn_3O_4/CeO_2/C$ (38.7 m^2g^{-1}) is lower than that of CeO_2/C (86.4 m^2g^{-1}) and higher than that of α-$MnO_2/Mn_3O_4/C$ (19.9 m^2g^{-1}). However, it is noteworthy that the inclusive ORR/OER electrocatalytic performance is not predominantly inspired by specific surface area

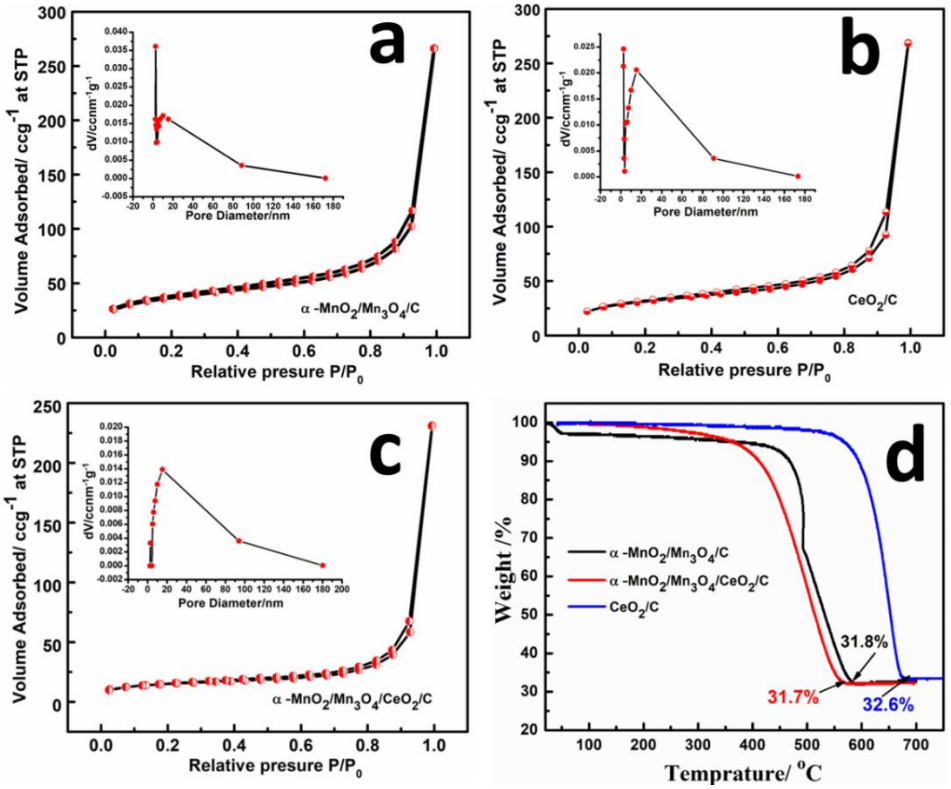

Figure 6.6. N_2 adsorption-desorption isotherms of (a) α-MnO_2/Mn_3O_4/C, (b) CeO_2/C and (c) α-MnO_2/Mn_3O_4/CeO_2/C hybrid (the inset displays the corresponding pore size distribution curves), and (d) TGA profile of α-MnO_2/Mn_3O_4/C, α-MnO_2/Mn_3O_4/CeO_2/C and CeO_2/C in air atmosphere.

of ECs. The TGA analysis shows the decay of carbon mass from the ECs as a function of temperature (Figure 6.6. d). It is observed that the TGA curves get stable after the loss of ~70 wt% which is due to the decomposition of carbon mass into CO_2 at higher temperatures. The remaining ~30 wt.% is the MO fraction which establishes the intended 30 wt% MO mass loading in the ECs systems.

6.2.2. Electrocatalytic Activity

The ORR activities of the synthesized nanostructures were first evaluated by CV in both N_2- and O_2-saturated 0.1M KOH solution on a GC electrode (Figure 6.7. a). The redox peaks observed in the CVs under O_2 saturated environment are exclusively due to the redox reaction of O_2 only, as under the N_2-saturated atmosphere no significant redox peak was observed. All the ECs (i.e., α-

$MnO_2/Mn_3O_4/C$, α-$MnO_2/Mn_3O_4/CeO_2/C$ and CeO_2/C) show significant electrocatalytic activity towards ORR. It is noteworthy that the incorporation of CeO_2 into α-$MnO_2/Mn_3O_4/C$ made the hybrid EC different in action towards electrocatalytic activity, CV loop, onset potential as well as peak potential. The ORR onset potential for α-$MnO_2/Mn_3O_4/C$ and CeO_2/C were found to be −0.15 V and −0.21 V (vs. Ag/AgCl), respectively while for α-$MnO_2/Mn_3O_4/CeO_2/C$ hybrid, it was observed to be −0.13 V (vs. Ag/AgCl). The observed positive shift suggests the overpotential drop for ORR with α-$MnO_2/Mn_3O_4/CeO_2/C$. Similarly, ORR peak potential for α-$MnO_2/Mn_3O_4/CeO_2/C$ shows a significant positive shift as compared to that shown by α-$MnO_2/Mn_3O_4/C$ and CeO_2/C. The primary assessment of ORR activity by CV study shows the significant promotion effect of CeO_2 in α-$MnO_2/Mn_3O_4/C$.

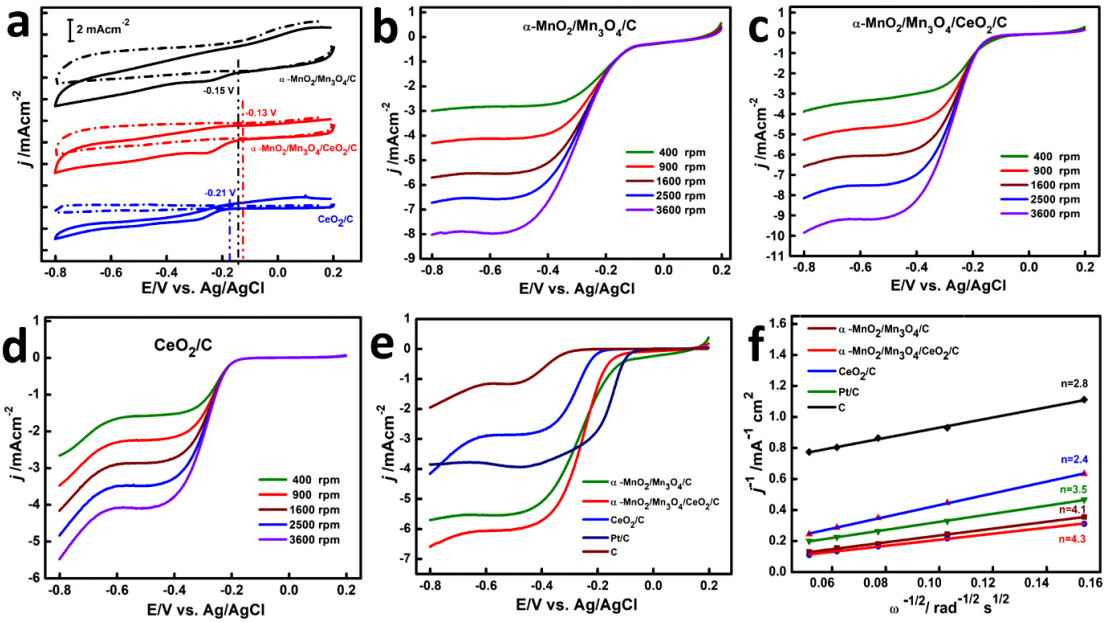

Figure 6.7. a) CVs of α-$MnO_2/Mn_3O_4/C$, α-$MnO_2/Mn_3O_4/CeO_2/C$ and CeO_2/C hybrid in N_2 (dash-dotted lines) and O_2 (solid lines) saturated 0.1 M KOH solution at a scan rate of 50 mV s^{-1}, b-d) ORR polarization curves of α-$MnO_2/Mn_3O_4/C$, α-$MnO_2/Mn_3O_4/CeO_2/C$ and CeO_2/C in O_2-saturated 0.1 M KOH solution at a sweep rate of 5 mV s^{-1}; e) ORR polarization curves of different ECs at 1600 rpm, f) K−L plots of different samples at −0.50 V (vs. Ag/AgCl).

To further explore the ORR pathways and the kinetics catalyzed by the prepared ECs, RDE measurements were performed. Figure 6.7. (b-d) presents the LSV polarization curves measured at different rpm in O_2 saturated 0.1 M KOH solution. The trends in the electrocatalytic activity of the ECs are comparable to those found in the CV study. Figure 6.7.e presents the LSV curves portraying the comparison of current densities and onset potentials for the investigated samples at 1600rpm. It is observed that Vulcan carbon shows a very weak electrocatalytic ORR activity, while the incorporation of α-MnO_2/Mn_3O_4 results in a more positive onset potential (−0.15 V). Interestingly, the α-MnO_2/Mn_3O_4/CeO_2/C hybrid shows more positive onset potential (−0.13 V) and half-wave potential (−0.24 V) which is reasonably higher than those of α-MnO_2/Mn_3O_4/C and CeO_2/C indicating a promotional effect after the addition of CeO_2. The limiting current density of α-MnO_2/Mn_3O_4/CeO_2/C at 1600 rpm is −6.63 mA cm^{-2} which is much higher than those of α-MnO_2/Mn_3O_4/C (−5.70 mA cm^{-2}), CeO_2/C (−4.14 mA cm^{-2}) and commercial Pt/C (−3.82 mA cm^{-2}).

Notably, the oxygen vacancy density in α-MnO_2/Mn_3O_4/CeO_2/C is lower than that of CeO_2/C because Ce^{3+} content is reduced somewhat in α-MnO_2/Mn_3O_4/CeO_2/C as suggested by XPS deconvolution analysis. However, mixed α-MnO_2/Mn_3O_4/CeO_2/C with adequate oxygen vacancies exhibits much better electrocatalytic performance than those of α-MnO_2/Mn_3O_4/C and CeO_2/C indicating the formation of more active sites in the mixed EC. The higher electrochemically active surface area (ECSA) of the mixed α-MnO_2/Mn_3O_4/CeO_2/C (39.4 m^2g^{-1}) might be working a significant role in enhanced ORR processes. Thus, the higher number of electrochemically active sites populated in α-MnO_2/Mn_3O_4/CeO_2/C hybrid may be readily accessible to O_2, building a remarkable contribution to boosting catalytic activities [58]. Moreover, CeO_2 could assist as a multifunctional component in the EC. Being an effective 'oxygen buffer', CeO_2 controls the reversible transportation of adequate O_2 into the active sites [59]. Therefore, the significantly enhanced activity can be ascribed to the strong synergistic interaction between α-MnO_2/Mn_3O_4 and CeO_2 [60].

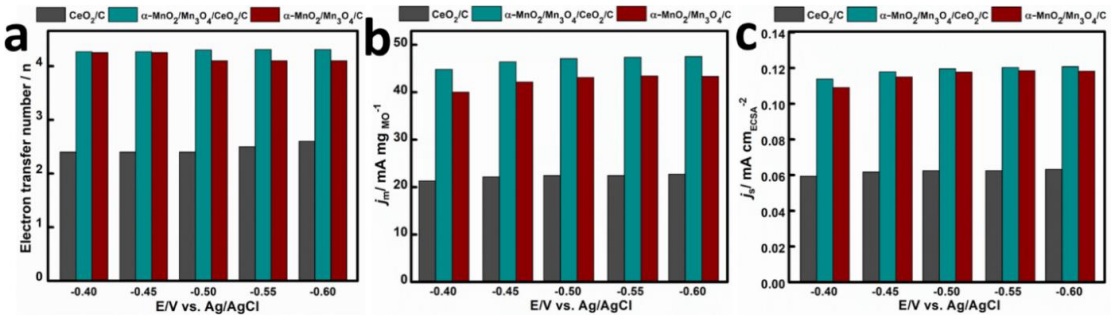

Figure 6.8. Electrocatalytic ORR performance of α-MnO_2/Mn_3O_4/C, α-MnO_2/Mn_3O_4/CeO_2/C and CeO_2/C. a) the number of electrons transferred at various potentials; b) mass-specific activity and c) specific activity.

The linear fitting lines of the K-L plots at −0.50 V are presented in Figure 6.7. f. Based on the K-L slope it is found that electrocatalysis over α-MnO_2/Mn_3O_4/C and α-MnO_2/Mn_3O_4/CeO_2/C proceeds via $4e^-$ pathway signifying a direct $4e^-$ oxygen reduction, without the formation of any O_2^{2-} intermediate. The electron transfer numbers (n) of Vulcan carbon, α-MnO_2/Mn_3O_4/C, CeO_2/C and Pt/C (20 wt. %) at −0.50 V are calculated to be 2.8, 4.1, 2.4 and 3.5, respectively. The linearity and parallel fitting lines of the K-L plots at diffusion-controlled and mixed kinetic diffusion-controlled potential regions of the LSV curves recommend first-order kinetics of the studied ORR ECs [61,62]. These observations further suggest a similar number of electrons transferred at all recorded RDE rotations during the ORR for the respective ECs. The average numbers of electrons transferred in the ORR process over a wide potential, ranging from −0.4 to −0.60 V (vs. Ag/AgCl) were also evaluated from the slopes of K-L plots as shown in Figure 6.8. a. The ECSA of the samples is evaluated by employing CV derived double layer capacitance (C_{dl}) method at a non-faradaic potential region (Figure 6.9.). The ECSA of α-MnO_2/Mn_3O_4/C, α-MnO_2/Mn_3O_4/CeO_2/C and CeO_2/C are calculated to be 36.6, 39.4 and 35.8 m^2g^{-1} respectively. The intrinsic activity of the ECs was measured based on the specific activity which is the current per unit ECSA. Mass activity and the over a potential range of −0.40 to −0.60 V is presented in Figure 6.8. (b and c). The mass activity and specific activity follow the order α-MnO_2/Mn_3O_4/CeO_2/C > α-MnO_2/Mn_3O_4/C > CeO_2/C over the investigated potential range for the set of ECs. The analogy between MA and SA concludes a significant mark regarding the intrinsic electrocatalytic

activity of α-MnO_2/Mn_3O_4/CeO_2/C. However, the variable amounts of CeO_2 in the mixed EC may decrease the ORR performance due to the lower intrinsic catalytic activity of CeO_2 in contrast to α-MnO_2/Mn_3O_4 [1].

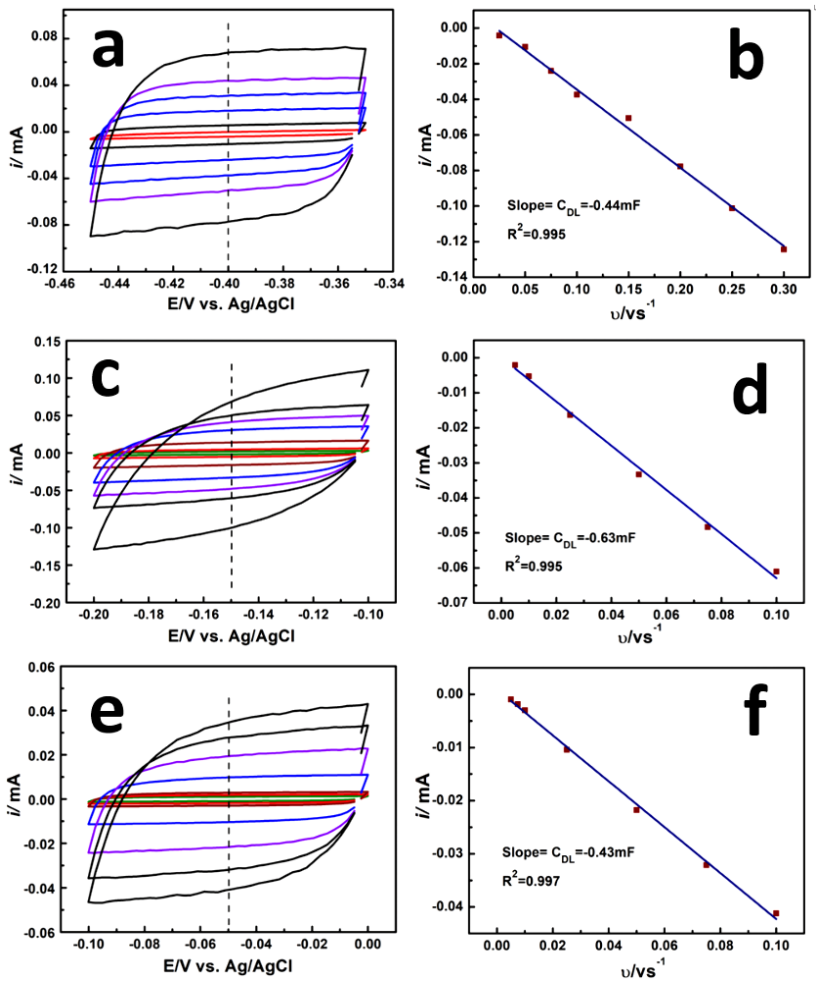

Figure 6.9. C_{dl} measurements for determining ECSA in 0.1 M KOH. The left panel (a, c, e) represents CVs of α-MnO_2/Mn_3O_4/C, α-MnO_2/Mn_3O_4/CeO_2/C and CeO_2/C at various scan rates. The right panel (b, d, f) is the slope obtained from respective CV data.

Therefore, to study the effect of CeO_2 on oxygen electrocatalysis, we have assessed the activity exhibited by α-MnO_2/Mn_3O_4/CeO_2/C-37 and α-MnO_2/Mn_3O_4/CeO_2/C-73 EC where the mixed hybrid is synthesized by changing the molar mass ratio of precursor salt. Figure 6.10. (a-e) shows the ORR activities exhibited by ECs α-MnO_2/Mn_3O_4/CeO_2/C-37 and α-MnO_2/Mn_3O_4/CeO_2/C-73. Figure 6.10.e portrays the effect of CeO_2 on ORR activity in terms of current density. The

obtained overall ORR performance along with specific activities, current densities and n values in the reaction process is significantly reduced for both the lower and higher CeO_2 concentration.

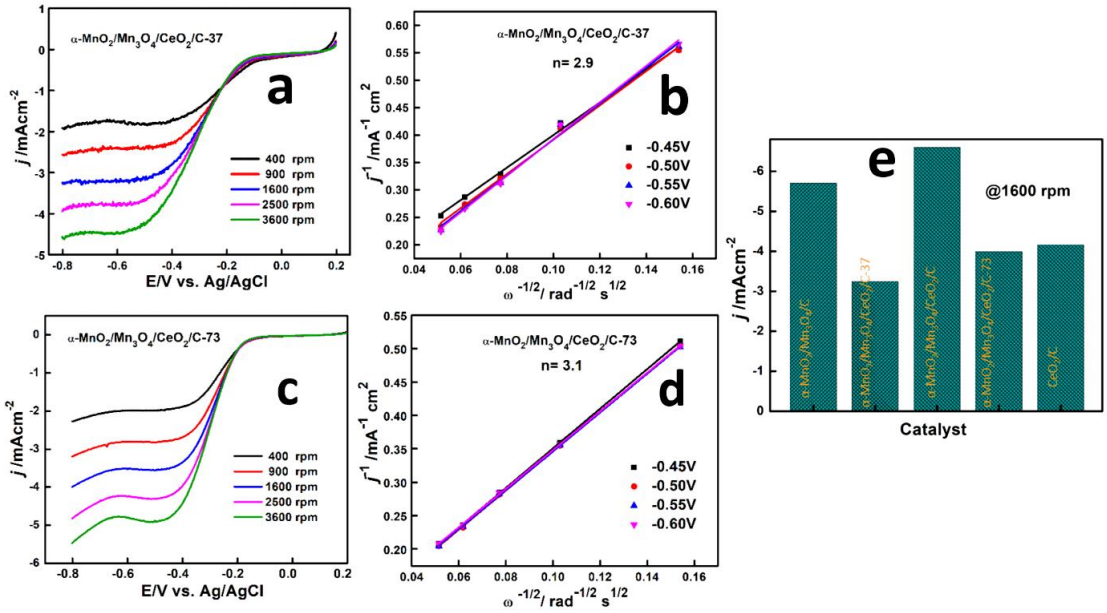

Figure 6.10. a, b) LSV curves of in O_2-saturated 0.1 M KOH @10 mV/s scan rate at different rpm and K-L plot for α-MnO_2/Mn_3O_4/CeO_2/C-37, respectively, c, d) LSV curves and K-L plot for α-MnO_2/Mn_3O_4/CeO_2/C-73, respectively and e) limiting current densities of the ECs at 1600 rpm.

Thus, the inclusive study suggests that an equilibrium Ce/Mn ratio is essentially significant for upholding the synergy that can enhance the ORR process which is exclusively satisfied by α-MnO_2/Mn_3O_4/CeO_2/C EC. The elemental analysis was further investigated by the EDX technique to confirm the CeO_2 content (Figure 6.2. and Table 6.1.). The intimate and overlapping interfacial contact between α-MnO_2/Mn_3O_4 and CeO_2 particles as observed from the HR-TEM images would also be instructive for the process of ORR enhancement. Notably, CeO_2 particles increase the degree of dispersion of α-MnO_2/Mn_3O_4 and simultaneously activate the O_2 directly involved in the redox processes. For instance, it is reported that CeO_2 in M_xO_y−CeO_2 composite could store and transport electrons to the adsorbed moieties such as NO, CO, O_2, etc. employing the resident Ce 4f orbital electrons [63,64]. The adsorbed moiety over CeO_2 could be readily activated which might improve the catalytic activity of the EC. Therefore, the high ECSA, high specific surface area,

reasonable oxygen vacancies, fascinating interfacial contact and strong synergistic interaction of Vulcan carbon with the equal molar ratio of α-MnO_2/Mn_3O_4 and CeO_2 could be the key factors that enhance the ORR performance of α-MnO_2/Mn_3O_4/CeO_2/C.

To assess the ORR kinetics, the corresponding Tafel plots are evaluated from the ORR LSV curves. Figure 6.11. a presents the Tafel slopes for the investigated ECs calculated at the high overpotential regions. The α-MnO_2/Mn_3O_4/CeO_2/C exhibits the lowest Tafel slope (921.9 mV dec^{-1}) at the high overpotential region suggesting a better kinetic current for ORR at the respective region. In addition, EIS measurements were performed to further study the kinetics and to identify the resistance of EC deposited electrodes performed in 0.1 M KOH solution within the frequency range from 6.2 MHz to 530 Hz.

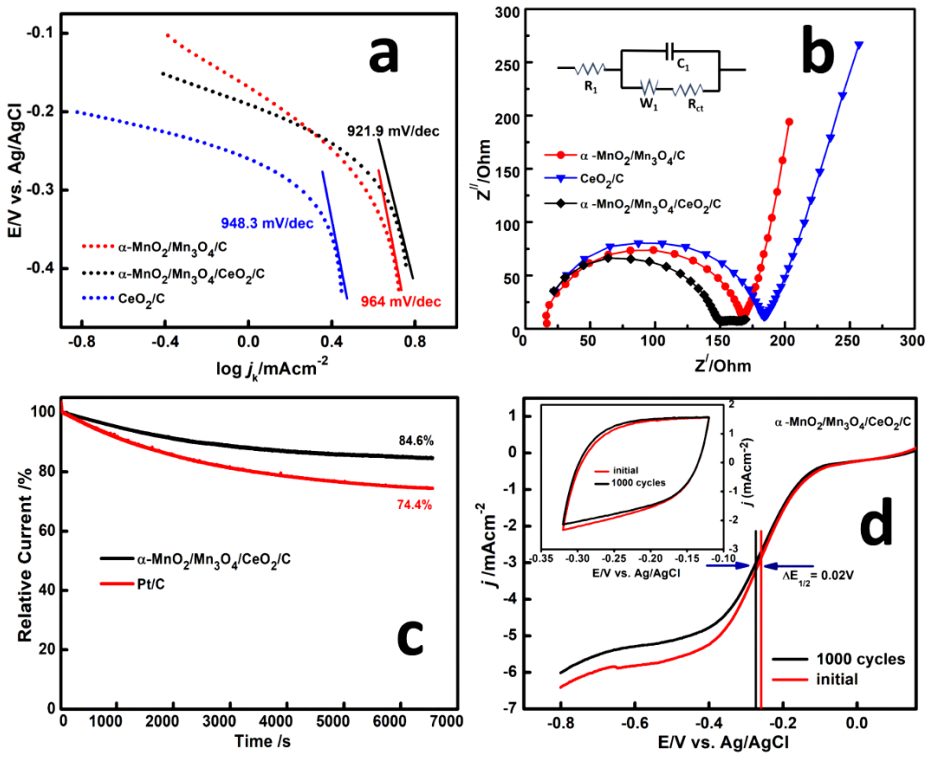

Figure 6.11. ORR kinetics, durability, and stability of α-MnO_2/Mn_3O_4/CeO_2/C hybrid nanostructure. a) Tafel plots, and b) Nyquist plots of α-MnO_2/Mn_3O_4/C, α-MnO_2/Mn_3O_4/CeO_2/C and CeO_2/C (inset of Figure b shows the equivalent circuit used for fitting the experimental data), c) chronoamperometric test for α-MnO_2/Mn_3O_4/CeO_2/C and Pt/C, and d) LSV plots of activity retention test after 1000 redox cycles.

The EIS profile is fitted according to an equivalent circuit (inset of Figure 6.11b), where R_1, W_1, R_{ct} and C_1 are the ohmic resistance, Warburg impedance, charge transfer resistance and double layer capacitance, respectively. The Nyquist plots show $Z^{/}$ (real part) vs. $Z^{//}$ (imaginary part) of the cell impedance for the investigated ECs (Figure 6.11.b). A characteristic semi-circle is observed for all the EC in the high-frequency region. The semicircle radius signifies the charge transfer resistance (R_{ct}) of the electrode-electrolyte interface system. It is observed that the calculated R_{ct} value of α-MnO_2/Mn_3O_4/CeO_2/C (132 Ω) is lower than that of α-MnO_2/Mn_3O_4/C (151.6 Ω) and CeO_2/C (164.4 Ω). It suggests that the α-MnO_2/Mn_3O_4/CeO_2/C extends faster charge transfer at the electrode-electrolyte interface and imparts high electrocatalytic activity toward ORR/OER [65,66]. The chronoamperometric (CA) test is presented in Figure 6.11. c illustrates the durability with percentage degradation of current in comparison to that of (20wt %) Pt/C. The CA test was performed for α-MnO_2/Mn_3O_4/CeO_2/C and Pt/C (20wt %) EC at 1600 rpm in 0.1 M KOH solution for 7000 seconds. CA test of α-MnO_2/Mn_3O_4/CeO_2/C EC in comparison with Pt/C reveals much better durability of α-MnO_2/Mn_3O_4/CeO_2/C EC than that of state-of-the-art Pt/C EC. Thus, the comprehensive evaluation of ORR activity in this work demonstrates the significant promotion effect of CeO_2 in the α-MnO_2/Mn_3O_4/C EC. Along with electrochemical activity, we comprehensively compared the durability and stability of α-MnO_2/Mn_3O_4/CeO_2/C EC with benchmark Pt/C EC, as these two parameters are vital for practical applications. The stability of α-MnO_2/Mn_3O_4/CeO_2/C EC was tested for 1000 redox cycles in O_2 saturated 0.1 M KOH solution at a scan rate of 100 mV s^{-1}. The LSV polarization curves were taken before and after 1000 redox cycles (Figure 6.11. d). The current density difference was observed to be too less as shown in Figure 6.11. d, and also the difference in half-wave potential $\Delta E_{1/2}$ is significantly smaller (0.02 V) suggesting superior stability exhibited by the EC. The LSV curves of the initial sample and that after 1000 redox cycles further signify the better retention of activity throughout the catalytic process.

We have tested the OER activity to study the water oxidation property over the EC surface. Figure 6.12. a shows ORR and OER activities of α-MnO_2/Mn_3O_4/CeO_2/C, Pd/C and Pt/C ECs investigated through LSV polarography analysis in 0.1 M KOH at 1600 rpm. An ideal OER EC should possess low

overpotential with high current densities available at low cost to be practically used in an industrial process. The OER onset potential for α-MnO_2/Mn_3O_4/CeO_2/C hybrid is 0.58V (vs. Ag/AgCl) which is lower than Pt/C (0.65V vs. Ag/AgCl) and Pd/C (0.75V vs. Ag/AgCl). Furthermore, the limiting current density of α-MnO_2/Mn_3O_4/CeO_2/C hybrid at a certain potential of 0.80V is 8.36 mA cm^{-2} which is far better than those of α-MnO_2/Mn_3O_4/C (6.77 mA cm^{-2}), α-MnO_2/Mn_3O_4/CeO_2/C-37 (2.4 mA cm^{-2}), α-MnO_2/Mn_3O_4/CeO_2/C-73(4.55 mA cm^{-2}), CeO_2/C (2.5 mA cm^{-2}), Pt/C (5.6 mA cm^{-2}) and Pd/C (1.2 mA cm^{-2}).

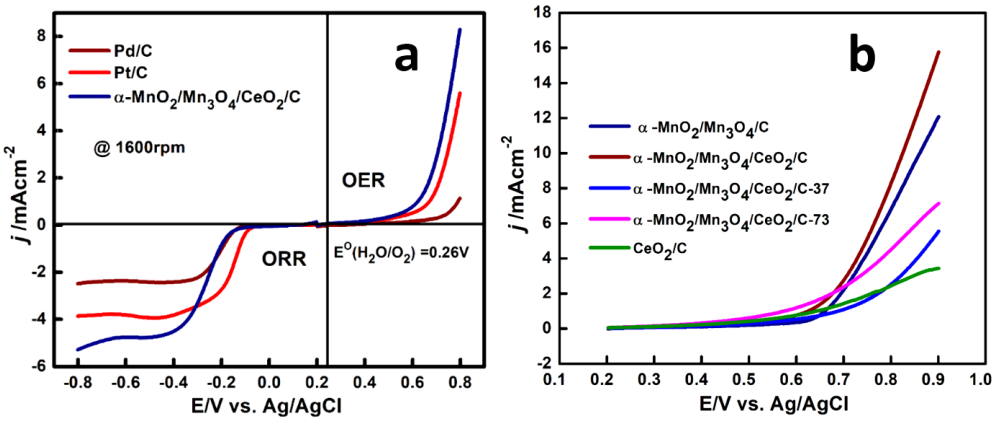

Figure 6.12. a) ORR and OER activities of α-MnO_2/Mn_3O_4/CeO_2/C compared with Pd/C and Pt/C, b) OER LSV curves of the ECs.

The OER activity for all investigated ECs is presented in Figure 6.12. b. Thus, EC α-MnO_2/Mn_3O_4/CeO_2/C shows much better OER activity with appreciable onset potential possessing very lower overpotential as compared to activity shown by all other investigated ECs. The enhanced OER activity could be attributed to the unique surface properties, higher oxygen vacancy densities, higher ECSA and the synergistic action of CeO_2, α-MnO_2/Mn_3O_4 and carbon. The overpotential within the effective ORR and OER range is a particularly crucial factor for evaluating the electrocatalytic bifunctionality toward ORR and OER [67,68]. The observed lesser overpotential between ORR and OER indicates that α-MnO_2/Mn_3O_4/CeO_2/C EC can function as a suitable reversible oxygen electrode EC.

The comparison of electrocatalytic performance with some previously reported MO-based materials is presented in Table 6.3. The ORR/OER activities shown by the α-MnO_2/Mn_3O_4/CeO_2/C hybrid observed to be superior to some recently reported ECs. For instance, ORR onset potential and $E_{1/2}$ values

Table 6.3. Comparison of ORR/OER activity of α-MnO_2/Mn_3O_4/CeO_2/C with analogous reported catalysts*

Catalysts	ORR		OER		ΔE/V [E(j_{10})–$E_{1/2}$)]	References
	E_{onset}/V	$E_{1/2}$/V	E(j_{10})/V	E_{onset}/V		
MnO_x–CeO_2/KB	–0.02	–0.15	–	–	–	[22]
Co_3O_4–CeO_2/KB	–0.01	–0.13	–	–	–	[44]
P-MnO_x-20	–0.09	–0.13	–	–	–	[69]
MnO_x	–0.07	–0.21	–	–	–	[70]
MnO_x/NC	–0.01	–0.16	0.71	0.45	0.87	[71]
MnO_x/C	–0.1	–0.32	0.74	0.49	1.06	[71]
MnO_x-Red/C	–0.20	–0.30	–	–	–	[72]
CuO/graphene	–0.20	–0.49	–	–	–	[73]
fluorinated copper manganese oxide (FCMO)	–0.26	–0.45	0.79	0.57	1.24	[74]
α-MnO_2/Mn_3O_4/CeO_2/C	–0.13	–0.24	0.82	0.58	1.06	This work

* Potential values are calculated as V vs. Ag/AgCl. The reported potentials were converted to the Ag/AgCl scale according to the Nernst equation: $E_{RHE} = E_{Ag/AgCl} + E^o_{Ag/AgCl} + 0.059$ pH, where E_{RHE} is the reversible hydrogen electrode potential, $E^o_{Ag/AgCl} = 0.1976$ at 25 °C, and $E_{Ag/AgCl}$ is converted potential vs. Ag/AgCl.

of α-MnO_2/Mn_3O_4/CeO_2/C hybrid are superior to CuO/graphene and fluorinated copper manganese oxide (FCMO) [73,74]. In addition, the overall bifunctional activity of α-MnO_2/Mn_3O_4/CeO_2/C hybrid, which can be evaluated as E(j_{10})–$E_{1/2}$ are observed to be close to the reported ECs. Moreover, the electrocatalytic activities in terms of current density, mass-specific activity, redox stability and durability for α-MnO_2/Mn_3O_4/CeO_2/C hybrid are significant which make the hybrid nanostructure a potential EC toward ORR/OER.

The typical ORR/OER mechanism in an active site of α-MnO_2/Mn_3O_4/CeO_2/C is depicted in Scheme 2. Many reports have explained that the ORR takes place on Mn^{3+} by two different preferential routes: the direct $4e^-$ route and the HO_2^-route. In both cases, the first step associates the transformation of Mn^{4+} to Mn^{3+} followed by the adsorption of molecular oxygen onto the electrochemically active sites. The electronic transformation on active sites of α-MnO_2/Mn_3O_4 is described by the following reactions [1,75,76].

$$Mn^{4+} + e^- \rightarrow Mn^{3+}$$

$$Mn^{2+} + Mn^{4+} \rightarrow 2Mn^{3+}$$

$$2Mn^{3+} + O_2 \rightarrow [Mn^{3+}]_2\ldots O_{2,ads}$$

$$[Mn^{3+}]_2\ldots O_{2,ads} + 2H_2O + 4e^- \rightarrow 4OH^- + [Mn^{3+}]_2\ldots O_{2,ads}$$

It is noteworthy that activation of ORR at a high-current density might be sometimes controlled by the sluggish diffusion of molecular oxygen into the electrochemically active surface sites [77]. CeO_2 owing to having rich oxygen vacancies has the exceptional capability of oxygen storage, transport and release [78–80]. The mechanism can be shown with the following equation [54]:

$$CeO_2 \leftrightarrow CeO_{2-x} + (x/2)\ O_2 \quad (0 \leq x \leq 0.5)$$

The equation shows that there exists a unique and delicate balance between Ce^{3+} and Ce^{4+} states and due to which CeO_2 can act as an oxygen buffer. It can reserve O_2 in an O_2-rich atmosphere and release it in O_2-deficiency conditions. Throughout the Ce^{4+}/Ce^{3+} redox process, this unique property of CeO_2 has great significance to the enhanced electrocatalytic performance in agreement with the Mars−Van Krevelen redox mechanism [44].

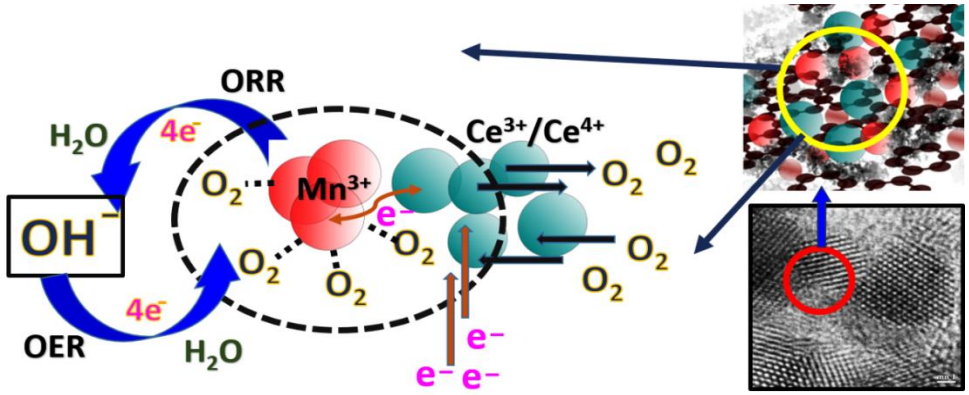

Scheme 6.1. Schematic illustration of α-MnO_2/Mn_3O_4/CeO_2/C catalyzed ORR and OER.

Thus, when the concentration of O_2 gets lower in the high-current density region, the adsorbed O_2 on CeO_2 sites accept electrons and form HO_2^-, followed by transfer to the proximate Mn_3O_4 active sites. In brief, the transfer of O_2 from the bulk O_2 to Mn^{3+} active sites via CeO_2 in the hetero-nanostructure demonstrated the

effective activation of molecular O_2 as depicted in Scheme 6.1. Furthermore, higher ECSA of the α-MnO_2/Mn_3O_4/CeO_2/C might exhibit significantly higher reaction sites of O_2 at a three-phase boundary. Therefore, efficient molecular O_2 activation due to the synergy between CeO_2 and α-MnO_2/Mn_3O_4 and the high ECSA enlighten the explanations for the enhanced performance of the cathode with the α-MnO_2/Mn_3O_4 /CeO_2/C EC under high discharge current density.

6.3. Conclusions

We utilized solvothermal route to fabricate α-MnO_2/Mn_3O_4/CeO_2/C hybrid nanostructure as an advanced bifunctional EC for ORR and OER in an alkaline media. Although α-MnO_2/Mn_3O_4/C and CeO_2/C individually exhibit oxygen electrocatalytic performance to some extent, the hybrid nanostructure (α-MnO_2/Mn_3O_4/CeO_2/C) displayed remarkable and astonishingly high ORR/OER performance in terms of current density at low overpotential with high stability and durability. All the electrocatalytic assessments are compared with the benchmark Pt/C and that reveals much better performance by the α-MnO_2/Mn_3O_4/CeO_2/C. This work introduces a highly promising EC for alkaline fuel cells with high efficiency, stability and durability as a suitably low-cost material. The promising ORR/OER activity of α-MnO_2/Mn_3O_4/CeO_2/C is likely due to sensibly originated nanostructure with synergistically active Mn (II/III/IV) multi-states sites conjugated with Ce (III/IV). The far-reaching hetero-structure and interfacial electro-conductive interaction make α-MnO_2/Mn_3O_4/CeO_2/C a potential EC towards ORR/OER. The strategy further offers an insightful approach to non-noble material design and advancements to the renewable energy scientific community.

References

[1] Tang, Y., Qiao, H., Wang, H., and Tao, P. Nanoparticulate $Mn_{0.3}Ce_{0.7}O_2$: A novel electrocatalyst with improved power performance for metal/air batteries. *Journal of Materials Chemistry A*, 1(40):12512-12518, 2013.

[2] Zhang, H., Qiao, H., Wang, H., Zhou, N., Chen, J., Tang, Y., Li, J. and Huang, C. Nickel cobalt oxide/carbon nanotubes hybrid as a high-

performance electrocatalyst for metal/air battery. *Nanoscale*, 6(17):10235-10242, 2014.

[3] Wu, D., Wei, Y., Ren, X., Ji, X., Liu, Y., Guo, X., Liu, Z., Asiri, A.M., Wei, Q. and Sun, X. $Co(OH)_2$ nanoparticle-encapsulating conductive nanowires array: room-temperature electrochemical preparation for high-performance water oxidation electrocatalysis. *Advanced Materials*, 30(9):1705366, 2018.

[4] Fournier, J., Faubert, G., Tilquin, J. Y., Guay, D., and Dodelet, J. P. High-performance, low Pt content catalysts for the electroreduction of oxygen in polymer-electrolyte fuel cells. *Journal of the Electrochemical Society*, 144(1):145, 1997.

[5] Song, C.; Zhang, J. Electrocatalytic Oxygen Reduction Reaction. In Zhang, J. editor(s), *PEM Fuel Cell Electrocatalysts and EC Layers: Fundamentals and Applications*, page: 89–134. ISBN: 978-1-84800-936-3, Springer London, 2008.

[6] Liang, J., Wang, Y., Liu, Q., Luo, Y., Li, T., Zhao, H., Lu, S., Zhang, F., Asiri, A.M., Liu, F. and Ma, D. Electrocatalytic hydrogen peroxide production in acidic media enabled by NiS_2 nanosheets. *Journal of Materials Chemistry A*, 9:6117-6122, 2021.

[7] Chen, G., Bare, S.R., and Mallouk, T.E. Development of supported bifunctional electrocatalysts for unitized regenerative fuel cells, *Journal of the Electrochemical Society*, 149(8):A1092, 2002.

[8] Zhao, A., Masa, J., Xia, W., Maljusch, A., Willinger, M.G., Clavel, G., Xie, K., Schlögl, R., Schuhmann, W., and Muhler, M. Spinel Mn-Co oxide in N-doped carbon nanotubes as a bifunctional electrocatalysts synthesized by oxidative cutting, *Journal of the American Chemical Society*, 136(21):7551-7554, 2014.

[9] Ledendecker, M., Clavel, G., Antonietti, M., and Shalom, M. Highly porous materials as tunable electrocatalysts for the hydrogen and oxygen evolution reaction, *Advanced Functional Materials*, 25(3):393-399, 2015.

[10] Aijaz, A., Masa, J., Rösler, C., Xia, W., Weide, P., Botz, A.J.R., Fischer, R.A., Schuhmann, W., and Muhler, M. $Co@Co_3O_4$ Encapsulated in carbon nanotube-grafted nitrogen-doped carbon polyhedra as an advanced

bifunctional oxygen electrode, *Angewandte Chemie International Edition,* 55(12):4087-4091, 2016.

[11] Stamenkovic, V., Mun, B.S., Mayrhofer, K.J.J., Ross, P.N., Markovic, N.M., Rossmeisl, J., Greeley, J., and Nørskov, J.K. Changing the activity of electrocatalysts for oxygen reduction by tuning the surface electronic structure, *Angewandte Chemie International Edition,* 118(18):2963-2967, 2006.

[12] Srivastava, R., Mani, P., Hahn, N., and Strasser, P. Efficient oxygen reduction fuel cell electrocatalysis on voltammetrically dealloyed Pt-Cu-Co nanoparticles, *Angewandte Chemie International Edition,* 46(47):8988-8991, 2007.

[13] Morozan, A., Jousselme, B., and Palacin, S. Low-platinum and platinum-free catalysts for the oxygen reduction reaction at fuel cell cathodes. *Energy & Environmental Science,* 4(4):1238-1254, 2011.

[14] Li, J., Mao, S., Hou, Y., Lei, L., and Yuan, C. 3D Edge-enriched Fe_3C@C nanocrystals with a core–shell structure grown on reduced graphene oxide networks for efficient oxygen reduction reaction. *ChemSusChem,* 11(18): 3292-3298, 2018.

[15] Katsounaros, I., Cherevko, S., Zeradjanin, A. R., and Mayrhofer, K. J. Oxygen electrochemistry as a cornerstone for sustainable energy conversion. *Angewandte Chemie International Edition,* 53(1):102-121, 2014.

[16] Gorlin, Y., and Jaramillo, T. F. A bifunctional nonprecious metal catalyst for oxygen reduction and water oxidation. *Journal of the American Chemical Society*, 132(39):13612-13614, 2010.

[17] Nugent, J. M., Santhanam, K. S. V., Rubio, A. A., and Ajayan, P. M. Fast electron transfer kinetics on multiwalled carbon nanotube microbundle electrodes. *Nano Letters*, 1(2):87-91, 2001.

[18] Yuan, C., Wu, H. B., Xie, Y., and Lou, X. W. Mixed transition-metal oxides: Design, synthesis, and energy-related applications. *Angewandte Chemie International Edition*, 53(6):1488-1504, 2014.

[19] Zhang, Z., Liu, J., Gu, J., Su, L., and Cheng, L. An overview of metal oxide materials as electrocatalysts and supports for polymer electrolyte fuel cells. *Energy & Environmental Science, 7*(8):2535-2558, 2014.

[20] Dresp, S., and Strasser, P. Non-Noble Metal oxides and their application as bifunctional catalyst in reversible fuel cells and rechargeable air batteries. *ChemCatChem*, 10(18):4162-4171, 2018.

[21] Meng, Y., Song, W., Huang, H., Ren, Z., Chen, S. Y., and Suib, S. L. Structure–property relationship of bifunctional MnO_2 nanostructures: Highly efficient, ultra-stable electrochemical water oxidation and oxygen reduction reaction catalysts identified in alkaline media. *Journal of the American Chemical Society*, 136(32):11452-11464, 2014.

[22] Chen, J., Zhou, N., Wang, H., Peng, Z., Li, H., Tang, Y., and Liu, K. Synergistically enhanced oxygen reduction activity of MnO_x–CeO_2/Ketjenblack composites. *Chemical Communications*, 51(50):10123-10126, 2015.

[23] Lambert, T. N., Vigil, J. A., White, S. E., Delker, C. J., Davis, D. J., Kelly, M Brumbach, M.T., Rodriguez, M.A. and Swartzentruber, B.S. Understanding the effects of cationic dopants on α-MnO_2 oxygen reduction reaction electrocatalysis. *The Journal of Physical Chemistry C*, 121(5):2789-2797, 2017.

[24] Ryabova, A. S., Napolskiy, F. S., Poux, T., Istomin, S. Y., Bonnefont, A., Antipin, D. M., Baranchikov, A.Y., Levin, E.E., Abakumov, A.M., Kéranguéven, G. and Antipov, E.V. Rationalizing the influence of the Mn (IV)/Mn (III) Red-Ox transition on the electrocatalytic activity of manganese oxides in the oxygen reduction reaction. *Electrochimica Acta*, 187:161-172, 2016.

[25] Lv, X., Lv, W., Wei, W., Zheng, X., Zhang, C., Zhi, L., and Yang, Q. H. A hybrid of holey graphene and Mn_3O_4 and its oxygen reduction reaction performance. *Chemical Communications*, 51(18):3911-3914, 2015.

[26] Paulus, U. A., Schmidt, T. J., Gasteiger, H. A., and Behm, R. J. Oxygen reduction on a high-surface area Pt/Vulcan carbon catalyst: A thin-film rotating ring-disk electrode study. *Journal of Electroanalytical Chemistry*, 495(2):134-145, 2001.

[27] Kuroda, S., Tobori, N., Sakuraba, M., and Sato, Y. Charge–discharge properties of a cathode prepared with ketjen black as the electro-conductive

additive in lithium-ion batteries. *Journal of Power Sources*, 119:924-928, 2003.

[28] Li, W., Wang, X., Chen, Z., Waje, M., and Yan, Y. Carbon nanotube film by filtration as cathode catalyst support for proton-exchange membrane fuel cell. *Langmuir*, 21(21):9386-9389, 2005.

[29] Chen, L., Xu, X., Yang, W., and Jia, J. Recent advances in carbon-based electrocatalysts for oxygen reduction reaction. *Chinese Chemical Letters*, 31(3):626-634, 2020.

[30] Hazarika, K. K., Goswami, C., Saikia, H., Borah, B. J., and Bharali, P. Cubic Mn_2O_3 nanoparticles on carbon as bifunctional electrocatalyst for oxygen reduction and oxygen evolution reactions. *Molecular Catalysis*, 451:153-160, 2018.

[31] Sudarsanam, P., Hillary, B., Amin, M. H., Rockstroh, N., Bentrup, U., Brückner, A., and Bhargava, S. K. Heterostructured copper–ceria and iron–ceria nanorods: Role of morphology, redox, and acid properties in catalytic diesel soot combustion. *Langmuir*, 34(8):2663-2673, 2018.

[32] Goswami, C., Yamada, Y., Matus, E. V., Ismagilov, I. Z., Kerzhentsev, M., and Bharali, P. Elucidating the role of oxide–oxide/carbon interfaces of CuO_x–CeO_2/C in boosting electrocatalytic performance. *Langmuir*, 36(49): 15141-15152, 2020.

[33] Louie, M. W., and Bell, A. T. An investigation of thin-film Ni–Fe oxide catalysts for the electrochemical evolution of oxygen. *Journal of the American Chemical Society*, 135(33):12329-12337, 2013.

[34] Wu, Z. P., Lu, X. F., Zang, S. Q., and Lou, X. W. Non-noble-metal-based electrocatalysts toward the oxygen evolution reaction. *Advanced Functional Materials*, 30(15):1910274, 2020.

[35] Qiu, F., Shi, J., Guo, M., Chen, S., Xia, J., and Lu, Z. H. Rapid synthesis of large-size Fe_2O_3 nanoparticle decorated NiO nanosheets via electrochemical exfoliation for enhanced oxygen evolution electrocatalysis. *Inorganic Chemistry*, 60(2):959-966, 2020.

[36] Xu, Z., Zhao, H., Liang, J., Wang, Y., Li, T., Luo, Y., Shi, X., Lu, S., Feng, Z., Wu, Q. and Sun, X. Noble-metal-free electrospun nanomaterials as

electrocatalysts for oxygen reduction reaction. *Materials Today Physics*, 15:100280, 2020.

[37] Mukherjee, D., and Reddy, B. M. Noble metal-free CeO_2-based mixed oxides for CO and soot oxidation. *Catalysis Today*, 309:227-235, 2018.

[38] Saikia, H., Hazarika, K. K., Chutia, B., Choudhury, B., and Bharali, P. A simple chemical route toward high surface area CeO_2 nanoparticles displaying remarkable radical scavenging activity. *ChemistrySelect*, *2*(11):3369-3375, 2017.

[39] Reddy, B. M., Bharali, P., Saikia, P., Park, S. E., van den Berg, M. W., Muhler, M., and Grünert, W. Structural characterization and catalytic activity of nanosized $Ce_xM_{1-x}O_2$ (M= Zr and Hf) mixed oxides. *The Journal of Physical Chemistry C*, 112(31):11729-11737, 2008.

[40] Jampaiah, D., Venkataswamy, P., Tur, K.M., Ippolito, S.J., Bhargava, S.K., and Reddy, B.M. Effect of MnO_x loading on structural, surface, and catalytic properties of CeO_2-MnO_x mixed oxides prepared by sol-gel method, *Zeitschrift für Anorganische und Allgemeine Chemie*, 641:1141–1149, 2015.

[41] Jampaiah, D., Velisoju, V. K., Devaiah, D., Singh, M., Mayes, E. L., Coyle, V. E., Reddy, B.M., Bansal, V. and Bhargava, S.K. Flower-like Mn_3O_4/CeO_2 microspheres as an efficient catalyst for diesel soot and CO oxidation: synergistic effects for enhanced catalytic performance. *Applied Surface Science*, 473:209-221, 2019.

[42] Masuda, T., Fukumitsu, H., Fugane, K., Togasaki, H., Matsumura, D., Tamura, K., Nishihata, Y., Yoshikawa, H., Kobayashi, K., Mori, T. and Uosaki, K. Role of cerium oxide in the enhancement of activity for the oxygen reduction reaction at Pt–CeO_x nanocomposite electrocatalyst-an in situ electrochemical X-ray absorption fine structure study. *The Journal of Physical Chemistry C*, 116(18):10098-10102, 2012.

[43] Yousaf, A. B., Imran, M., Uwitonze, N., Zeb, A., Zaidi, S. J., Ansari, T. M., Yasmeen, G. and Manzoor, S. Enhanced electrocatalytic performance of Pt3Pd1 alloys supported on CeO_2/C for methanol oxidation and oxygen reduction reactions. *The Journal of Physical Chemistry C*, 121(4):2069-2079, 2017.

[44] Liu, K., Huang, X., Wang, H., Li, F., Tang, Y., Li, J., and Shao, M. Co_3O_4–CeO_2/C as a highly active electrocatalyst for oxygen reduction reaction in Al–air batteries. *ACS Applied Materials & Interfaces*, 8(50):34422-34430, 2016.

[45] Lee, J. S., Park, G. S., Lee, H. I., Kim, S. T., Cao, R., Liu, M., and Cho, J. Ketjenblack carbon supported amorphous manganese oxides nanowires as highly efficient electrocatalyst for oxygen reduction reaction in alkaline solutions. *Nano Letters*, 11(12):5362-5366, 2011.

[46] McBride, J. R., Hass, K. C., Poindexter, B. D., and Weber, W. H. Raman and x-ray studies of $Ce_{1-x}RE_xO_{2-y}$, where RE= La, Pr, Nd, Eu, Gd, and Tb. *Journal of Applied Physics*, 76(4):2435-2441, 1994.

[47] Zhang, X., Wei, J., Yang, H., Liu, X., Liu, W., Zhang, C., and Yang, Y. One-pot synthesis of Mn-doped CeO_2 nanospheres for CO oxidation. *European Journal of Inorganic Chemistry*, 2013(25):4443-4449, 2013.

[48] Qian, W., Chen, Z., Cottingham, S., Merrill, W. A., Swartz, N. A., Goforth, A. M., Clare, T.L. and Jiao, J. Surfactant-free hybridization of transition metal oxide nanoparticles with conductive graphene for high-performance supercapacitor. *Green Chemistry*, 14(2):371-377, 2012.

[49] Jia, J., Zhang, P., and Chen, L. The effect of morphology of α-MnO_2 on catalytic decomposition of gaseous ozone. *Catalysis Science & Technology*, 6(15):5841-5847, 2016.

[50] Arani, H. F., Mirhabibi, A. R., Collins, S., Daroughegi, R., Soltani, A. K., Naghizadeh, R., Riahi-Noori, N., Aghababazadeh, R. and Westwood, A. Enhancement in graphitization of coal tar pitch by functionalized carbon nanotubes. *RSC Advances*, 7(9):5533-5540, 2017.

[51] Wang, Z., Shen, G., Li, J., Liu, H., Wang, Q., and Chen, Y. Catalytic removal of benzene over CeO_2–MnO_x composite oxides prepared by hydrothermal method. *Applied Catalysis B: Environmental*, 138:253-259, 2013.

[52] Huang, Z., Zhou, W., Ouyang, C., Wu, J., Zhang, F., Huang, J., Gao, Y. and Chu, J. High performance of Mn-Co-Ni-O spinel nanofilms sputtered from acetate precursors. *Scientific Reports*, 5(1):1-8, 2015.

[53] Jampaiah, D., Tur, K. M., Venkataswamy, P., Ippolito, S. J., Sabri, Y. M., Tardio, J., Bhargava, S.K. and Reddy, B.M. Catalytic oxidation and

adsorption of elemental mercury over nanostructured CeO_2–MnO_x catalyst. *RSC Advances*, 5(38):30331-30341, 2015.

[54] Picasso, G., Gutiérrez, M., Pina, M. P., and Herguido, J. Preparation and characterization of Ce-Zr and Ce-Mn based oxides for n-hexane combustion: Application to catalytic membrane reactors. *Chemical Engineering Journal*, *126*(2-3):119-130, 2007.

[55] Wang, Z., Wang, W., Zhang, L., and Jiang, D. Surface oxygen vacancies on Co_3O_4 mediated catalytic formaldehyde oxidation at room temperature. *Catalysis Science & Technology*, 6(11):3845-3853, 2016.

[56] Nguyen, T. D., Dinh, C. T., and Do, T. O. Monodisperse samarium and cerium orthovanadate nanocrystals and metal oxidation states on the nanocrystal surface. *Langmuir*, 25(18):11142-11148, 2009.

[57] Zhang, L., and Shen, Y. One-pot synthesis of platinum–ceria/graphene nanosheet as advanced electrocatalysts for alcohol oxidation. *ChemElectroChem*, 2(6):887-895, 2015.

[58] Zhou, X., Bai, Z., Wu, M., Qiao, J., and Chen, Z. 3-Dimensional porous N-doped graphene foam as a non-precious catalyst for the oxygen reduction reaction. *Journal of Materials Chemistry A*, *3*(7):3343-3350, 2015.

[59] Balducci, G., Islam, M. S., Kašpar, J., Fornasiero, P., and Graziani, M. Reduction process in CeO_2−MO and CeO_2−M_2O_3 mixed oxides: A computer simulation study. *Chemistry of Materials*, 15(20):3781-3785, 2003.

[60] Li, S. S., Cong, H. P., Wang, P., and Yu, S. H. Flexible nitrogen-doped graphene/carbon nanotube/Co_3O_4 paper and its oxygen reduction activity. *Nanoscale*, 6(13):7534-7541, 2014.

[61] Xia, W., Mahmood, A., Liang, Z., Zou, R., and Guo, S. Earth-abundant nanomaterials for oxygen reduction. *Angewandte Chemie International Edition*, 55(8):2650-2676, 2016.

[62] Wang, M., Huang, J., Wang, M., Zhang, D., Zhang, W., Li, W., and Chen, J. Co_3O_4 nanorods decorated reduced graphene oxide composite for oxygen reduction reaction in alkaline electrolyte. *Electrochemistry Communications*, 34:299-303, 2013.

[63] Baron, M., Abbott, H., Bondarchuk, O., Stacchiola, D., Uhl, A., Shaikhutdinov, S., Freund, H.J., Popa, C., Ganduglia-Pirovano, M.V. and

Sauer, J. Resolving the atomic structure of vanadia monolayer catalysts: monomers, trimers, and oligomers on ceria. *Angewandte Chemie International Edition*, 48(43):8006-8009, 2009.

[64] Zhu, W. J., Zhang, J., Gong, X. Q., and Lu, G. A density functional theory study of small Au nanoparticles at CeO_2 surfaces. *Catalysis Today*, 165(1):19-24, 2011.

[65] He, L., Liu, J., Liu, Y., Cui, B., Hu, B., Wang, M., Tian, K., Song, Y., Wu, S., Zhang, Z. and Peng, Z. Titanium dioxide encapsulated carbon-nitride nanosheets derived from MXene and melamine-cyanuric acid composite as a multifunctional electrocatalyst for hydrogen and oxygen evolution reaction and oxygen reduction reaction. *Applied Catalysis B: Environmental*, 248:366-379, 2019.

[66] Shi, J., Qiu, F., Yuan, W., Guo, M., and Lu, Z. H. Nitrogen-doped carbon-decorated yolk-shell CoP@ FeCoP micro-polyhedra derived from MOF for efficient overall water splitting. *Chemical Engineering Journal*, 403:126312, 2021.

[67] Jung, J. I., Jeong, H. Y., Lee, J. S., Kim, M. G., and Cho, J. A bifunctional perovskite catalyst for oxygen reduction and evolution. *Angewandte Chemie International Edition*, 53(18):4582-4586, 2014.

[68] Masa, J., Xia, W., Sinev, I., Zhao, A., Sun, Z., Grützke, S., Weide, P., Muhler, M. and Schuhmann, W. MnxOy/NC and CoxOy/NC nanoparticles embedded in a nitrogen-doped carbon matrix for high-performance bifunctional oxygen electrodes. *Angewandte Chemie International Edition*, 53(32):8508-8512, 2014.

[69] Vigil, J. A., Lambert, T. N., Kelly, M., and Aidun, R. Hybrid PEDOT/MnO x nanostructured electrocatalysts for oxygen reduction. *Materials Chemistry Frontiers*, 1(8):1668-1675, 2017.

[70] Cheng, Y., Dou, S., Saunders, M., Zhang, J., Pan, J., and Wang, S. A class of transition metal-oxide@ MnO_x core–shell structured oxygen electrocatalysts for reversible O_2 reduction and evolution reactions. *Journal of Materials Chemistry A*, 4(36):13881-13889, 2016.

[71] Pandey, J., Hua, B., Ng, W., Yang, Y., van der Veen, K., Chen, J., Geels, N.J., Luo, J.L., Rothenberg, G. and Yan, N. Developing hierarchically porous

MnO_x/NC hybrid nanorods for oxygen reduction and evolution catalysis. *Green Chemistry*, 19(12):2793-2797, 2017.

[72] Li, Z., Yang, Y., Relefors, A., Kong, X., Siso, G. M., Wickman, B., Kiros, Y. and Soroka, I.L. Tuning morphology, composition and oxygen reduction reaction (ORR) catalytic performance of manganese oxide particles fabricated by γ-radiation induced synthesis. *Journal of Colloid and Interface Science*, 583:71-79, 2021.

[73] Yu, J., Huang, T., Jiang, Z., Sun, M., and Tang, C. A hybrid material combined copper oxide with graphene for an oxygen reduction reaction in an alkaline medium. *Molecules*, 24(3):441, 2019.

[74] Rai, V., Lee, K. P., Safanama, D., Adams, S., and Blackwood, D. J. Oxygen reduction and evolution reaction (ORR and OER) bifunctional electrocatalyst operating in a wide pH range for cathodic application in Li–Air batteries. *ACS Applied Energy Materials*, 3(9):9417-9427, 2020.

[75] Cao, Y. L., Yang, H. X., Ai, X. P., and Xiao, L. F. The mechanism of oxygen reduction on MnO_2-catalyzed air cathode in alkaline solution. *Journal of Electroanalytical Chemistry*, 557:127-134, 2003.

[76] Ominde, N., Bartlett, N., Yang, X. Q., and Qu, D. Investigation of the oxygen reduction reaction on the carbon electrodes loaded with MnO_2 catalyst. *Journal of Power Sources*, 195(13):3984-3989, 2010.

[77] Kostowskyj, M. A., Kirk, D. W., and Thorpe, S. J. Ag and Ag–Mn nanowire catalysts for alkaline fuel cells. *International Journal of Hydrogen Energy*, 35(11):5666-5672, 2010.

[78] Chang, L. H., Sasirekha, N., Chen, Y. W., and Wang, W. J. Preferential oxidation of CO in H_2 stream over Au/MnO_2−CeO_2 catalysts. *Industrial & Engineering Chemistry Research*, 45(14):4927-4935, 2006.

[79] Shi, L., Chu, W., Qu, F., and Luo, S. Low-temperature catalytic combustion of methane over MnO_x–CeO_2 mixed oxide catalysts: Effect of preparation method. *Catalysis Letters*, 113(1):59-64, 2007.

[80] Li, H., Qi, G., Zhang, X., Huang, X., Li, W., and Shen, W. Low-temperature oxidation of ethanol over a $Mn_{0.6}Ce_{0.4}O_2$ mixed oxide. *Applied Catalysis B: Environmental*, 103(1-2):54-61, 2011.